Assessment of Eccentricity for Multiple Nonmetallic Pipes Using Microwave Sensing

Yuki Gao, *Member, IEEE*, Maharshi B. Shah, and Reza K. Amineh, *Senior Member, IEEE*

***Abstract*— Double pipes are employed in various industrial sectors, such as oil and gas, mining, and fluid transfer. Normally, the pipes are assumed to be concentric, however, environmental factors may cause misalignment of their axes and cause the so-called eccentricity. This may affect other important parameters, such as flow rate, and burst pressure. Yet, there are limited studies on techniques for detecting and estimating the eccentricity. In this article, for the first time, we propose techniques to detect and estimate eccentricity in double nonmetallic pipes using microwave sensing. For this purpose, we employ an array of antennas scanning the pipes along the azimuthal direction. Receiver antennas with similar angular separations with respect to a transmitter antenna and on the opposite sides of that are assumed to have similar responses when the transmitter is on the eccentricity axis. Using such receiver responses, we demonstrate the possibility to detecting the axis eccentricity as well as estimating the eccentricity value by constructing an inversion curve *a priori*. The proposed method is validated through simulation and experimental results.**

***Index Terms*— Composite pipes, eccentricity, microwave sensing, nondestructive testing (NDT), nonmetallic pipes.**

I. Introduction

VARIOUS industrial sectors employ double pipes for different applications. Commonly, the pipes are concentric and aligned using centralizers, but there may be misalignments in their axes called eccentricity due to the environmental issues or other factors. For industries such as oil and gas, mining, and pipelines, the presence of eccentricity may be desirable or undesirable. With that being said, the study of eccentricity detection is crucial due to the effects it may cause on flow instability, burst pressure, acoustic physics, nondestructive testing (NDT) techniques, and so on. For example, drilling companies are in search of flow behavior and properties of drilling fluids. This is due to the fact that flow instability is a crucial parameter in the oil well drilling process as turbulent flow is desirable. Drill pipes tend to sag, which leads to annulus eccentricity affecting flow instability [1]. Furthermore, eccentricity affects the production of laminar vortex rings as previous studies have indicated a faster flow development with eccentric annulus [2]. Also, a small increase in eccentricity while other parameters are kept constant can reduce the average pipe wall shear stress and magnitude of the pressure gradient that is required [3]. In addition, a slight eccentricity can decrease the burst pressure [4]. Besides, for oil and gas wellbores, acoustic features, such as slowness dispersions and modal structures, are sensitive to the presence of casing eccentricity [5]. Finally, in [6], it has been shown that the presence of eccentricity can cause image deterioration when using microwave imaging for NDT of double pipes.

The usage of nonmetallic and composite pipes is rapidly taking over different industries due to advantages, such as low cost, lightweight, and resistance to corrosion [7]–[9]. Due to that, we envision the importance of detecting and evaluating the eccentricity in such pipes. However, traditional NDT techniques, such as eddy current, ultrasound testing, and radiography, cannot be used for inspection of nonmetallic pipes made of composite materials, such as fiber-reinforced plastic (FRP), high-density polyethylene (HDPE), polyvinyl chloride (PVC), and glass-reinforced epoxy resin (GRE). To bridge this gap, a microwave measurement approach has already been proposed as a promising technique for inspection of multiple nonmetallic pipes. Microwave NDT can help detect cracks, defects, and delamination in nonmetallic pipes. For instance, in [10], microwave NDT has been proposed for the inspection of GRE pipes using the *K*-band and *Ka*-band rectangular aperture probes at 18–26.5 GHz and 26.5–40 GHz, respectively. In [11], wideband synthetic aperture radar (SAR) imaging has been employed to produce the three-dimensional (3-D) images of vertical cracks/flaws in HDPE pipes. In addition, the SAR-based NDT method for multilayered cylindrical pipe structures has been proposed in [12]. In [13], a time-reversal SAR imaging method has been proposed for inspection of lossy symmetric and asymmetric multilayered dielectric cylindrical objects. Later, wideband near-field holographic imaging has been proposed for NDT of double concentric nonmetallic pipes [14]. Furthermore, in [15], holographic imaging has been proposed for imaging of multiple nonmetallic concentric pipes employing narrow frequency band with an array of receiver antennas. Recently, holographic imaging of double composite pipes with arrays of transmitter and receiver antennas has been proposed in [16] for faster data acquisition along the azimuthal direction. Lastly, terahertz waves (THz) have been used for

Manuscript received October 7, 2021; revised November 19, 2021; accepted November 27, 2021. Date of publication December 9, 2021; date of current version March 1, 2022. This work was supported in part by the U.S. National Science Foundation (NSF) under Award 1920098 and in part by the New York Institute of Technology's Institutional Support for Research and Creativity (ISRC) Grants. The Associate Editor coordinating the review process was Dr. Kristen M. Donnell. *(Corresponding author: Reza K. Amineh.)*

The authors are with the Department of Electrical and Computer Engineering, New York Institute of Technology, New York, NY 10023 USA (e-mail: rkhalaja@nyit.edu).

Digital Object Identifier 10.1109/TIM.2021.3134322

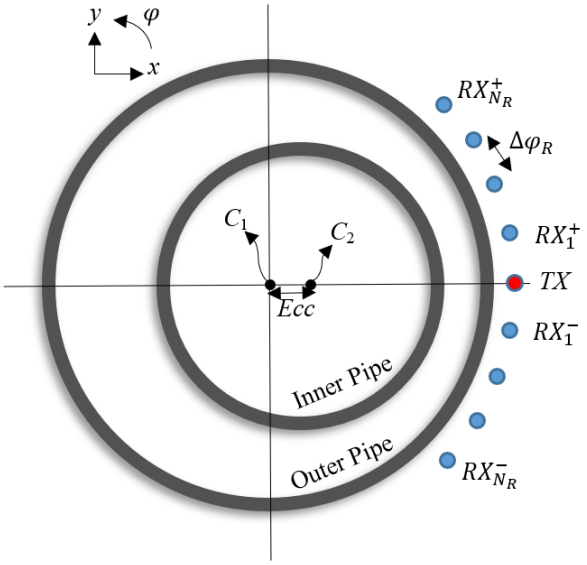

Fig. 1. Top view of double eccentric pipes with eccentricity E_{cc} between the center of the outer pipe, C_1, and the center of the inner pipe, C_2. Red circle and blue circles represent transmitter antenna and receiver antennas, respectively.

imaging of nonmetallic pipes as well. In [17], terahertz imaging for NDT testing of PVC pipe cap has been proposed where the received reflected signals have been analyzed to determine the thickness and location of the defects. In [18], THz waves reflection imaging and time-domain spectroscopy transmission modes have been employed to detect any electrofusion joint defects in polyethylene pipes. Besides, the application of terahertz signals for thickness measurement and defect detection in nonmetallic pipes for the oil and gas industry has been proposed in [19].

In this article, we use arrays of receiver antennas placed at azimuthally symmetric positions with respect to a single transmitter. The responses obtained from the receiver antennas are then processed via a fast and robust method to estimate the axis of eccentricity for double nonmetallic pipes. Such responses are also employed along with a preconstructed inversion curve to estimate the value of eccentricity as well. The performance of the proposed method is demonstrated through simulation and experimental results.

II. Principle

In this section, we present a method to detect and estimate the presence of eccentricity, E_{cc}, for a double nonmetallic pipes configuration using microwave sensing. Fig. 1 shows the top view of double pipes setup with axis eccentricity along the x-axis. The setup also consists of a transmitter antenna to illuminate the pipes and an array of receiver antennas to receive the scattered waves. The antennas are separated along the azimuthal direction by $\Delta\varphi_R$. Pairs of symmetrical receiver antennas are placed on the positive and negative angles, $\pm i\,\Delta\varphi_R$, $i = 1, \ldots, N_R$ with respect to the transmitter antenna and they are denoted by RX_i^{+} and RX_i^{-}, respectively.

To detect eccentricity, we scan the antenna array along the azimuthal direction φ from 0° to 180° (no need to scan a full circle since the structure is symmetrical with respect to the eccentricity axis) and we compute the difference, ΔR, in the responses of the ith receiver antenna pair, R_i^{+} and R_i^{-}, at each frequency f, as

$$\Delta R(\varphi, f) = R_i^{+}(\varphi, f) - R_i^{-}(\varphi, f). \tag{1}$$

The responses discussed in this article are the magnitudes of the transmission S-parameters measured for each receiver antenna. In (1), due to having a symmetrical structure with respect to the axis of eccentricity, we expect the minima of ΔR, $\Delta R_{\min}$, to occur at the angle where the transmitter antenna is on the axis of eccentricity. In theory, the elements in each receiver antenna pair are assumed to be identical. However, there are unavoidable differences between the elements of the receiver antenna pairs due to fabrication errors and so on. To reduce such differences, we obtain the calibrated responses $R_i^{\mathrm{cal}\pm}$ of the ith receiver antenna pair by dividing the eccentric configuration's responses $R_i^{e\pm}$ and concentric configuration's responses $R_i^{c\pm}$. This can be written as

$$R_i^{\mathrm{cal}\pm}(\varphi, f) = R_i^{e\pm}(\varphi, f)/R_i^{c\pm}(\varphi, f). \tag{2}$$

This division acts as a normalization process on the responses of individual antennas. For instance, if $R_i^{c+}(\varphi, f)$ is larger than $R_i^{c-}(\varphi, f)$, in practice (ideally, they should be equal due to the use of identical receiver antennas placed symmetrically with respect to the transmitter antenna in a concentric pipe configuration), using (2) compensates this undesired effect since $R_i^{e+}(\varphi, f)$ will be divided by a larger number. Then, using the calibrated responses $R_i^{\mathrm{cal}\pm}$, we modify (1) for a practical scenario as

$$\Delta R(\varphi, f) = \left|R_i^{\mathrm{cal}+}(\varphi, f) - R_i^{\mathrm{cal}-}(\varphi, f)\right| \tag{3}$$

where $|.|$ denotes the absolute value operator. It is worth noting that the calibration method in (2) is similar to the calibration approach used in imaging of concentric pipes in [16]. From (3), as discussed above, we first find $\Delta R_{\min}$, which occurs at $\varphi_{\min}$, where $\varphi_{\min}$ represents the axis of eccentricity. Also, we expect the maximum of ΔR, $\Delta R_{\max}$, over the axis, with angle of $\varphi_{\max}$, which is perpendicular to the axis of eccentricity (i.e., $\varphi_{\max} = \varphi_{\min} \pm 90°$). We employ $\Delta R_{\max}$ to estimate the eccentricity value as follows. We first conduct experiments with predetermined eccentricity values for the inner pipe and collect responses to obtain the corresponding $\Delta R_{\max}$ values. With the collected values, we construct an inversion curve relating $\Delta R_{\max}$ values to the eccentricity values for each receiver antenna pair. Then, in a test scenario, we estimate the eccentricity value by using $\Delta R_{\max}$ obtained from the measurement and the inversion curve constructed *a priori*.

To summarize the methodology, in the following, we provide the required steps for estimation of eccentricity value.

1) *Step 1:* Generate an inversion curve beforehand by measuring the responses for the pipes with predetermined eccentricity directions and values for the given setup.
2) *Step 2:* Measure the responses for a test scenario by scanning the antennas along the azimuthal direction (0°–180°).

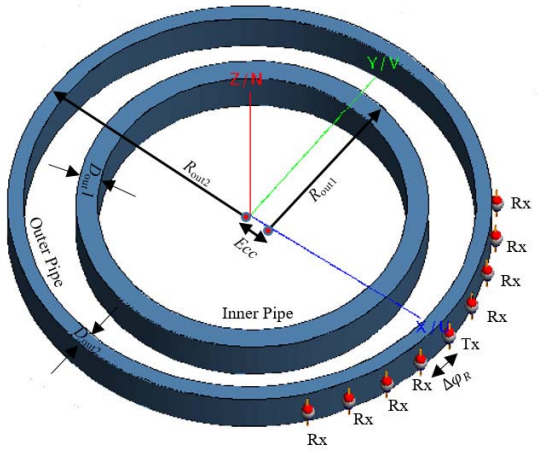

Fig. 2. Illustration of the simulation setup in FEKO [20].

3) *Step 3:* Find $\Delta R_{\min}$ from the measured responses, which occurs at $\varphi_{\min}$ ($\varphi_{\min}$ determines the axis of eccentricity).
4) *Step 4:* Find the value of $\Delta R_{\max}$ from the measured responses for the receiver pair $\mathrm{RX}_i^{\pm}$.
5) *Step 5:* Locate the value of $\Delta R_{\max}$ over the inversion curve constructed for receiver pair $\mathrm{RX}_i^{\pm}$ in step 1 and find the corresponding value of the eccentricity.

In general, the discussed methods can be performed by measuring responses over multiple frequencies and by multiple receiver antenna pairs where a final determination for the axis of eccentricity and estimation of eccentricity value can be obtained from the weighted average of the results. For instance, when using multiple frequencies, N_f, and one receiver antenna pair, we can average ΔR over frequencies, which is denoted by ΔR^{avg}. This can be written as

$$\Delta R^{\mathrm{avg}}(\varphi) = \frac{\sum_{i=1}^{N_f} \Delta R(\varphi, f_i)}{N_f}. \tag{4}$$

The value of $\Delta R_{\min}$ is then found from minimum of ΔR^{avg}, which determines the axis of eccentricity. Besides, the maximum of ΔR^{avg}, namely $\Delta R^{\mathrm{avg}}_{\max}$, can be employed for construction of the inversion curves (by measuring pipes with preknown eccentricities) and then employing them to estimate the eccentricity values as explained before.

III. Simulation Results

In this section, first, the performance of the proposed methods is demonstrated via simulations with FEKO [20]. Then, we present a parametric study to evaluate the effect of uncertainties in major parameters on the performance of the method.

A. Detection and Evaluation of Eccentricity

Fig. 2 shows an illustration of the simulation setup. Here, we try to detect and estimate eccentricity by using the setup with array of antennas placed on the outside of the outer pipe. There are nine antennas separated by an angular separation, $\Delta\varphi_R$, of 10° where one of them (the middle element) is a transmitter antenna and the rest are receiver antennas. The outer radii of the inner and outer pipes are $R_{\mathrm{out1}} = 57.5$ mm and $R_{\mathrm{out2}} = 79$ mm, respectively. The thicknesses of the inner and outer pipes are $D_{\mathrm{out1}} = 7$ mm and $D_{\mathrm{out1}} = 5$ mm, respectively. The two nonmetallic pipes are assumed to be made of PVC with an approximate relative permittivity ε_r of 2.25 and a tangent loss of 0.0004 [21]. Furthermore, the operation frequency is 10 GHz. Eccentricity is denoted by E_{cc} which is the distance between the center of the inner pipe and outer pipe, while the outer pipe is assumed to be concentric with respect to the array of antennas. We have four pairs of receiver antennas where $\mathrm{RX}_1^{\pm}$ are the closest to the transmitter antenna and $\mathrm{RX}_4^{\pm}$ are the farthest from the transmitter antenna. We implement the one-dimensional (1-D) scanning of the transmitter and receiver antennas along the azimuthal direction (φ) from 0° to 180° to acquire the responses. To mimic real-world scenarios, white Gaussian noise with a signal-to-noise ratio (SNR) of 25 dB is added to the simulated responses by applying the *awgn* command in MATLAB [22].

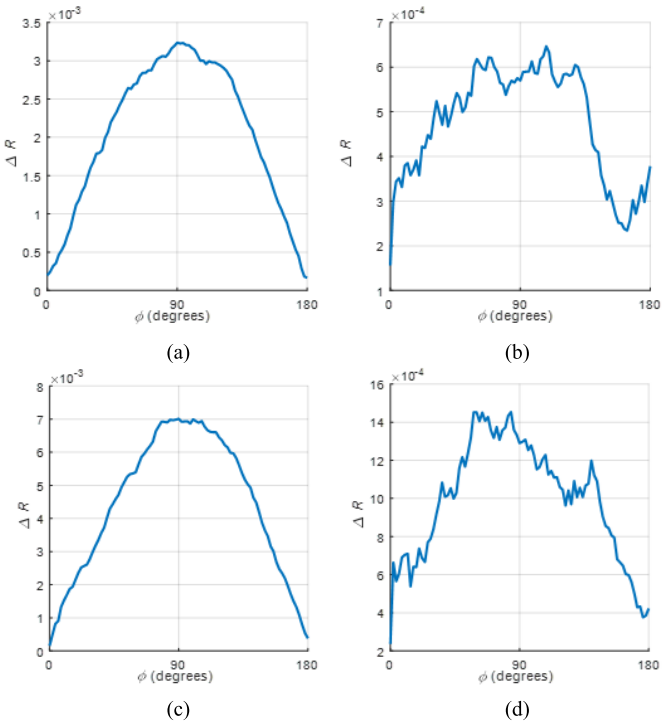

Fig. 3. Variations of ΔR when using (a) $R_4^{\pm}$ for $E_{\mathrm{cc}} = 0.5$ mm, (b) $R_1^{\pm}$ for $E_{\mathrm{cc}} = 0.5$ mm, (c) $R_4^{\pm}$ for $E_{\mathrm{cc}} = 1.1$ mm, and (d) $R_1^{\pm}$ for $E_{\mathrm{cc}} = 1.1$ mm.

We first demonstrate the method to detect the angle of eccentricity axis by applying predetermined eccentricity along the positive x-axis ranging from 0.5 to 1.9 mm with a step of 0.2 mm. Fig. 3 shows the variation of ΔR in (3) for $\mathrm{RX}_4^{\pm}$ and $\mathrm{RX}_1^{\pm}$ receiver antenna pairs and for E_{cc} values of 0.5 and 1.1 mm. In Fig. 3(a) and (c), it is observed that at angles of 0° and 180°, we can see the minima of ΔR. As discussed in Section II, this confirms that the axis of eccentricity is along the x-axis, which is correct. In addition, in Fig. 3(a) and (c), the maxima of ΔR occur at approximately 90° (this is perpendicular to the axis of eccentricity). This is expected according to the discussions in Section II. However, in Fig. 3(b) and (d), it is observed that the quality of ΔR vari-

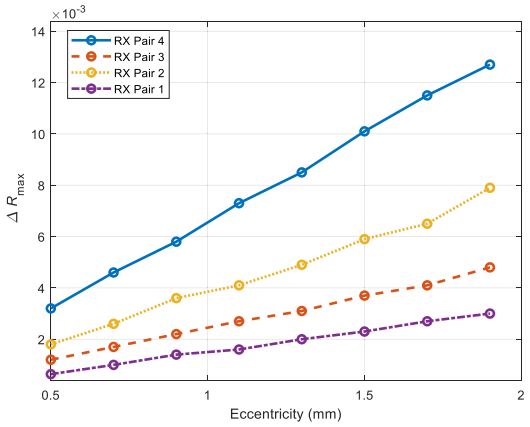

Fig. 4. Generated inversion curves. RX Pair i indicates using data of $\mathrm{RX}_i^{\pm}$.

ation is poor and locating $\Delta R_{\min}$ and $\Delta R_{\max}$ is not as robust as those in Fig. 3(a) and (c). This is due to the fact that $\mathrm{RX}_1^{\pm}$ have a shorter signal path difference in eccentric configuration compared to $\mathrm{RX}_4^{\pm}$ leading to smaller ΔR values (lower SNR for ΔR variation). According to our study, the detection of axis of eccentricity improves as the receiver antenna pairs are farther away from the transmitter antenna. Also, deduced from Fig. 3(a) and (c), as the value of eccentricity increases, there is a slight improvement in the detection of axis of eccentricity.

Then, for each receiver antenna pair, with the obtained maxima of ΔR, $\Delta R_{\max}$, for all predetermined eccentricity values E_{cc}, we construct an inversion curve, which can be employed to estimate eccentricity later. Fig. 4 shows the generated inversion curves. As expected, for all receiver antenna pairs, as E_{cc} value increases, $\Delta R_{\max}$ increases. In a test scenario, by evaluating $\Delta R_{\max}$ from the measured responses for $\mathrm{RX}_i^{\pm}$ and using the corresponding inversion curve, we can estimate the value of eccentricity. Alternatively, one can obtain the value of eccentricity by computing the weighted average of estimations obtained from multiple inversion curves when using responses for multiple receivers and/or at multiple frequencies.

B. Effects of Uncertainties in Major Parameters

In this section, we conduct a comprehensive study of the effect of uncertainties in major parameters, including standoff distance for the antennas, misalignment of antenna array with respect to the pipes, thickness of the pipes, and relative permittivity of the pipes. When studying the effect of each parameter, the rest of the parameters are kept the same as the reference setup discussed in Section III-A. From each scenario, with varying the studied parameter, the value of $\Delta R_{\max}$ is obtained and used along with the inversion curve for the reference setup to estimate the value of eccentricity. Also, the estimation error (in percentage) for each scenario is evaluated at the true eccentricities of 0.5, 1.1, and 1.9 mm using

$$\mathrm{Error} = \frac{\mathrm{True\,Eccentricity} - \mathrm{Estimated\,Eccentricity}}{\mathrm{True\,Eccentricity}} \times 100. \tag{5}$$

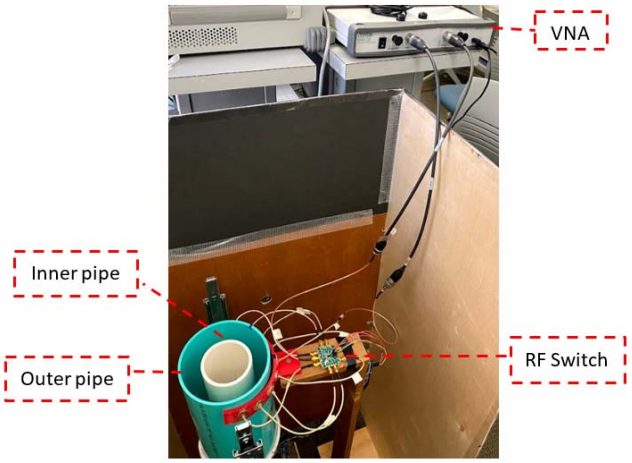

(a)

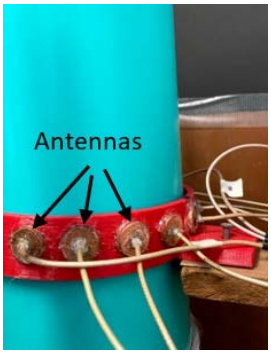

(b)

Fig. 5. (a) Main components of the microwave sensing system and (b) cavity-backed printed spiral antennas introduced in [15].

Table I shows the effect of changing the standoff distance from 2 to 3 mm by presenting the error between the true eccentricities and estimated eccentricities using various receiver antenna pairs. The error ranged between 0% and 13.5%. Table II shows the estimation error from the effect of misaligned antenna array with respect to the pipes (shifting of both pipes along the y-axis by 1 mm while keeping the z-axis as the antenna array axis). The error ranged from 0% to 10.53%. In general, the effect of misalignment between the antenna array and the pipes presented less error than the effect of changing the standoff distance. Furthermore, Table III shows the eccentricity estimation error when increasing the thickness of both pipes by 10% with respect to the reference setup. So far, among the studied scenarios, the errors presented in this table are higher and can reach up to 40%. Lastly, Table IV shows the variation of errors when relative permittivities of both pipes are increased by approximately 15% (from $\varepsilon_r = 2.25$ to $\varepsilon_r = 2.6$). Here, the errors are significantly higher at certain receiver antenna pairs where error reaches up to 230%. In general, this scenario presented the largest errors when using $\mathrm{RX}_3^{\pm}$, $\mathrm{RX}_2^{\pm}$, and $\mathrm{RX}_1^{\pm}$ compared to the other studied scenarios.

IV. Experimental Results

In this section, we present the experimental results to detect and estimate eccentricity. Fig. 5(a) shows the microwave

TABLE I

ESTIMATED ECCENTRICITIES AND THEIR CORRESPONDING ERRORS USING RESPONSES AT STANDOFF DISTANCE OF 3 mm AND THE INVERSION CURVE FROM THE REFERENCE SETUP

True Eccentricity	Estimated Eccentricity Using $RX_4^{\pm}$	Error (%)	Estimated Eccentricity Using $RX_3^{\pm}$	Error (%)	Estimated Eccentricity Using $RX_2^{\pm}$	Error (%)	Estimated Eccentricity Using $RX_1^{\pm}$	Error (%)
0.5 mm	0.47 mm	6%	0.46 mm	8%	0.5 %	0%	0.5 mm	0%
1.1 mm	0.98 mm	10.9%	1.02 mm	7.27%	1.02 mm	7.27%	1.15 mm	4.55%
1.9 mm	1.64 mm	13.5%	1.81 mm	4.52%	1.79 mm	6%	1.77 mm	6.84%

TABLE II

ESTIMATED ECCENTRICITIES AND THEIR CORRESPONDING ERRORS USING RESPONSES FOR MISALIGNED ANTENNA ARRAYS AND THE INVERSION CURVE FROM THE REFERENCE SETUP

True Eccentricity	Estimated Eccentricity Using $RX_4^{\pm}$	Error (%)	Estimated Eccentricity Using $RX_3^{\pm}$	Error (%)	Estimated Eccentricity Using $RX_2^{\pm}$	Error (%)	Estimated Eccentricity Using $RX_1^{\pm}$	Error (%)
0.5 mm	0.51 mm	2.8%	0.5 mm	0%	0.55 mm	10%	0.55 mm	10%
1.1 mm	1.15 mm	4.55%	1.1 mm	0%	1.18 mm	6.82%	1.13 mm	2.27%
1.9 mm	1.85 mm	2.63%	1.9 mm	0%	1.87 mm	1.53%	1.7 mm	10.53%

TABLE III

ESTIMATED ECCENTRICITIES AND THEIR CORRESPONDING ERRORS USING RESPONSES WITH INCREASED THICKNESSES FOR BOTH PIPES ($D_{\text{out1}} = 7.7$ mm AND $D_{\text{out1}} = 5.5$ mm) AND THE INVERSION CURVE FROM THE REFERENCE SETUP

True Eccentricity	Estimated Eccentricity Using $RX_4^{\pm}$	Error (%)	Estimated Eccentricity Using $RX_3^{\pm}$	Error (%)	Estimated Eccentricity Using $RX_2^{\pm}$	Error (%)	Estimated Eccentricity Using $RX_1^{\pm}$	Error (%)
0.5 mm	0.57 mm	17.2%	0.7 mm	40%	0.43 mm	15%	0.4 mm	20%
1.1 mm	1.12 mm	2.12%	1.55 mm	40.9%	0.86 mm	21.82%	0.8 mm	27.27%
1.9 mm	2.13 mm	12.32%	2.42 mm	27.11%	1.5 mm	21.05%	1.5 mm	21.05%

TABLE IV

ESTIMATED ECCENTRICITIES AND THEIR CORRESPONDING ERRORS USING RESPONSES WITH INCREASED RELATIVE PERMITTIVITY ($\varepsilon_r = 2.6$) FOR BOTH PIPES AND THE INVERSION CURVE FROM THE REFERENCE SETUP

True Eccentricity	Estimated Eccentricity Using $RX_4^{\pm}$	Error (%)	Estimated Eccentricity Using $RX_3^{\pm}$	Error (%)	Estimated Eccentricity Using $RX_2^{\pm}$	Error (%)	Estimated Eccentricity Using $RX_1^{\pm}$	Error (%)
0.5 mm	0.46 mm	8%	1.65 mm	230%	0.72 mm	44%	1.1 mm	120%
1.1 mm	0.94 mm	14.55%	3.05 mm	177%	1.46 mm	32.7%	2.05 mm	86.4%
1.9 mm	1.64 mm	13.53%	5.15 mm	171%	2.24 mm	17.9%	3.7 mm	94.7%

sensing system that consists of a transmitter antenna, eight receiver antennas, an Anritsu MS46122B vector network analyzer (VNA), an RF switch (EV1HMC321ALP4E from analog devices), two PVC pipes, a circular scanning system, a PC, and an Arduino Uno. The inner and outer pipes have the inner diameters of 76 mm (3 in) and 152 mm (6 in), respectively. Besides, the inner and outer pipes have the thicknesses of 6 and 5 mm, respectively. The operating frequency is from 6 to 8 GHz. We employ the cavity-backed printed spiral antennas proposed and used in [15] for this study. Fig. 5(b) shows the utilized antennas embedded inside the 3-D printed holder. For more information about the antennas, please refer to [15]. In [15], the array of these antennas was employed in a cylindrical scanning setup to provide data for holographic microwave imaging of double concentric pipes. The number of antennas is similar to the simulation study, but the angular separation between the antennas is 20° (due to the physical size of the antennas, angular separation of 10° is not feasible). In addition, similar to our simulation setup, we have four receiver antenna pairs, where $\text{RX}_1^{\pm}$ are the closest to and $\text{RX}_4^{\pm}$ are the farthest away from the transmitter antenna. The VNA is used to measure the magnitude of the transmission parameters for the receiver antennas and the RF switch is used to switch between the receiver antennas to collect the responses. To collect the responses along the azimuthal direction, the antennas are fixed, while the pipes are being rotated by the positioning system. This is to avoid the undesired interferences due to the motion of the microwave cables and so on. Furthermore, the room temperature was between 70 °F and 75 °F and the humidity was between 50% and 55%.

Here, we conduct experiments to detect the axis of eccentricity by first applying predetermined eccentricity values ranging from 2 to 10 mm with a step of 2 mm. We apply the method mentioned in Section II where we employ data acquired at ten frequency steps ranging from 6 to 8 GHz

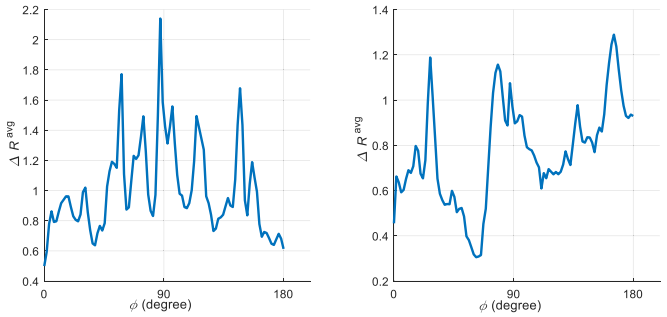

Fig. 6. Variations ΔR^{avg} for $E_{\text{cc}} = 4$ mm when using (a) $R_4^{\pm}$ and (b) $R_1^{\pm}$.

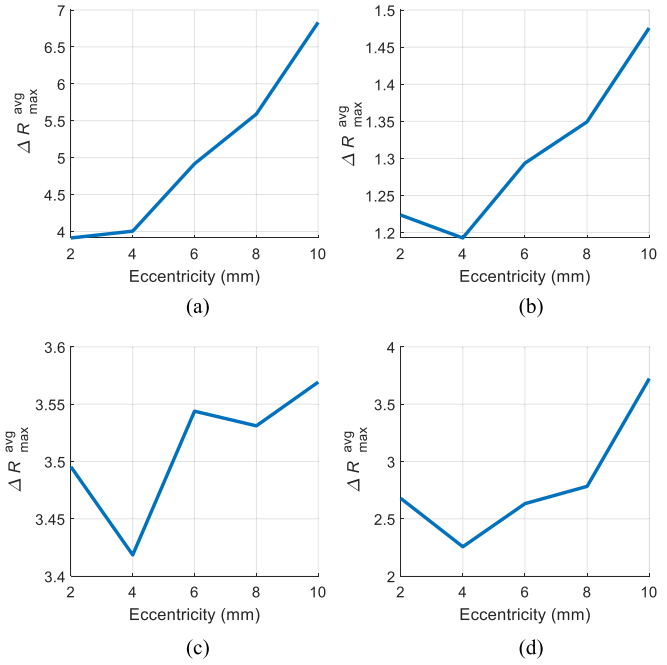

Fig. 7. Generated inversion curves for (a) $\text{RX}_4^{\pm}$, (b) $\text{RX}_3^{\pm}$, (c) $\text{RX}_2^{\pm}$, and (d) $\text{RX}_1^{\pm}$.

for every receiver antenna pair. Fig. 6 shows the difference of the calibrated ΔR^{avg} when using calibrated responses for $R_4^{\pm}$ and for $R_1^{\pm}$ at $E_{\text{cc}} = 4$ mm. In Fig. 6(a), it is observed that the minima of the calibrated ΔR^{avg} occur at 0° and 180° as expected. In other words, we can detect the axis of eccentricity as discussed in Section II. In addition, the maximum of the calibrated ΔR^{avg} occurs at approximately 90°, which is perpendicular to the axis of eccentricity. Yet, in Fig. 6(b), there are no minima of ΔR^{avg} at 0° and 180°. We believe that this is due to two effects. First, as discussed in the simulation study, due to smaller spatial difference, there is a smaller difference between signal paths for receiver antenna pair $\text{RX}_1^{\pm}$. Second, there is a direct coupling effect from transmitter antenna to the elements of the receiver antenna pairs that cannot be fully reduced by subtracting the calibrated responses in (3) because the elements in each receiver antenna pair are not exactly identical, in practice.

Furthermore, Fig. 7 shows the generated inversion curves for various receiver antenna pairs. Please note that Fig. 7(a) shows the most accurate inversion curve obtained for $\text{RX}_4^{\pm}$ where the value of $\Delta R_{\text{max}}^{\text{avg}}$ increases with the increase of E_{cc} monotonically. Overall, we observe that as the receiver antenna pairs get closer to the transmitter antenna, the correlation between $\Delta R_{\text{max}}^{\text{avg}}$ and E_{cc} degrades. As discussed in Section II, this is due to two factors: the shorter signal path difference between the receiver antennas in pair $\text{RX}_1^{\pm}$ and the effect of direct coupling between the transmitter and the receiver antennas for that pair.

V. Conclusion and Discussion

In this article, for the first time, we used a microwave sensing system in a double nonmetallic pipe configuration to detect and estimate eccentricity. Using this system, we employed the 1-D scanning along the azimuthal direction for the transmitter and receiver antennas that are placed at angularly symmetrical positions with respect to the transmitter antenna. Two receivers at opposite angular separations with respect to the transmitter antenna were referred to as a pair. In both simulation and experimental studies, we have tried to assess the effect of angular separation of the receiver antennas on the quality of the eccentricity detection/estimation. Due to this, we have employed multiple receiver pairs with various angular separations. However, we should emphasize that having only one pair of receiver antennas is sufficient to implement both eccentricity detection and estimation.

To detect the eccentricity axis, we utilized the minima in the difference of the calibrated responses for a receiver antenna pair. To estimate eccentricity, we employed the maxima in the difference of the calibrated responses for the pair and constructed an inversion curve with predetermined eccentric configurations. Such an inversion curve can be then used to estimate eccentricity in the later test scenarios.

From our study, it was observed that the detection of eccentricity axis is more accurate when the receiver antenna pair is farther away from the transmitter antenna. This is due to the larger spatial difference that causes a larger difference in the signal paths for the elements of the pair. Besides, there is a direct coupling effect between elements of the pair and the transmitter antenna, which cannot be completely reduced in experiments due to the unavoidable difference between antennas. This effect is more pronounced when the receiver antenna pair is closer to the transmitter antenna. In the simulation and experimental results, it was demonstrated that having angular separations of 40° and 80°, respectively, provides satisfactory results. Although having larger angular separation is normally desired, one must consider other factors such as possible attenuation of the received microwave power (in particular, when the pipes carry lossy fluids), which counteracts the positive effect of having larger angular separation on the eccentricity detection and estimation.

Furthermore, from the constructed inversion curves, it is observed that as eccentricity increases, the maximum in the difference of calibrated responses for the antenna pair increases as well. In general, it is noted that larger eccentricity values can be detected and estimated more reliably.

As it is common in the microwave sensing and imaging systems, the repeatability of the measurements in the proposed

setup can be affected by the movements and bending of the cables, the gap between the antennas and the pipes, outside interferences, and background objects in the scanning setup. In our experiments, we reduce the effect of cable movements and bending by securing them with zip ties to the scanning stand. Also, to keep the gap between the antennas and the pipes as fixed as possible, we tried our best to keep the rotary platform concentric with the antenna holder. Furthermore, to reduce the outside interferences, we placed our scanning setup in a box covered by microwave absorbing sheets. Finally, to minimize the effect of background objects in the scanning setup, we avoid additional changes in the setup from measurement to measurement.

Overall, to improve the proposed method, one can utilize the data obtained from multiple receiver antenna pairs and/or at multiple frequencies to obtain the weighted averaged result for the estimated eccentricity.

REFERENCES

[1] S. K. Dewangan, "Effect of eccentricity and inner pipe motion on flow instability for flow through annulus," *Social Netw. Appl. Sci.*, vol. 3, no. 4, p. 513, Mar. 2021.

[2] T. Asim, R. Mishra, and V. Rao, "Effect of eccentricity on pipe boundary layer growth for flows in annulus," in *Proc. Comput. Eng. Researcher's Conf.*, Mar. 2012, pp. 1–6.

[3] H. V. Moradi and S. Tavoularis, "Flow instability in weakly eccentric annuli," *Phys. Fluids*, vol. 31, no. 4, Apr. 2019, Art. no. 044104.

[4] Z. Chen, W. Zhu, Q. Di, and W. Wang, "Prediction of burst pressure of pipes with geometric eccentricity," *J. Pressure Vessel Technol.*, vol. 137, no. 6, Dec. 2015, Art. no. 061201.

[5] Y. Liu, R. M. D'Angelo, G. Choi, L. Zhu, S. Bose, and S. Zeroug, "Understanding acoustic physics in oil and gas wellbores with the presence of ubiquitous geometric eccentricity," in *Proc. AIP Conf.*, 2018, p. 1949.

[6] Y. Gao, N. Raisa, and R. Amineh, "Effect of eccentricity in microwave imaging of multiple composite pipes," *Columbia Undergraduate Sci. J.*, vol. 15, pp. 30–38, May 2021.

[7] R. Stakenborghs and J. Little, "Microwave based NDE inspection of HDPE pipe welds," in *Proc. 17th Int. Conf. Nuclear Eng. (ICONE)*, Jan. 2009, pp. 185–193.

[8] R. J. Stakenborghs, "Microwave inspection method and its application to FRP," in *Proc. MTI AmeriTAC Conf.*, 2013, pp. 1–41.

[9] A. G. Gibson, J. M. Linden, D. Elder, and K. H. Leong, "Non-metallic pipe systems for use in oil and gas," *Plastics, Rubber Compos.*, vol. 40, no. 10, pp. 465–480, Dec. 2013.

[10] M. S. U. Rahman, A. Haryono, Z. Akhter, and M. A. Abou-Khousa, "On the inspection of glass reinforced epoxy pipes using microwave NDT," in *Proc. IEEE Int. Instrum. Meas. Technol. Conf. (I MTC)*, May 2019, pp. 1–5.

[11] M. T. Ghasr, K. Ying, and R. Zoughi, "3D millimeter wave imaging of vertical cracks and its application for the inspection of HDPE pipes," in *Proc. AIP Conf.*, Jan. 2014, vol. 1581, no. 1, pp. 1531–1536.

[12] J. Laviada, B. Wu, M. T. Ghasr, and R. Zoughi, "Nondestructive evaluation of microwave-penetrable pipes by synthetic aperture imaging enhanced by full-wave field propagation model," *IEEE Trans. Instrum. Meas.*, vol. 68, no. 4, pp. 1112–1119, Apr. 2019.

[13] B. Wu, Y. Gao, J. Laviada, M. T. Ghasr, and R. Zoughi, "Time-reversal SAR imaging for nondestructive testing of circular and cylindrical multi-layered dielectric structures," *IEEE Trans. Instrum. Meas.*, vol. 69, no. 5, pp. 2057–2066, May 2020.

[14] R. K. Amineh, M. Ravan, and R. Sharma, "Nondestructive testing of nonmetallic pipes using wideband microwave measurements," *IEEE Trans. Microw. Theory Techn.*, vol. 68, no. 5, pp. 1763–1772, May 2020.

[15] H. Wu, M. Ravan, R. Sharma, J. Patel, and R. K. Amineh, "Microwave holographic imaging of nonmetallic concentric pipes," *IEEE Trans. Instrum. Meas.*, vol. 69, no. 10, pp. 7594–7605, Oct. 2020.

[16] Y. Gao, M. Ravan, and R. K. Amineh, "Fast, robust, and low-cost microwave imaging of multiple non-metallic pipes," *Electronics*, vol. 10, no. 15, p. 1762, Jul. 2021.

[17] L.-H. Kang and D.-H. Han, "Robotic-based terahertz imaging for non-destructive testing of a PVC pipe cap," *NDT E Int.*, vol. 123, Oct. 2021, Art. no. 102500.

[18] X. L. Liao, Y. L. Liu, and H. Wang, "Nondestructive evaluation of electrofusion joint of polyethylene pipeline using terahertz ray," in *Proc. Adv. Mater. Energy Sustainability*, 2017, pp. 213–219.

[19] M. Farhat, A. M. Amer, V. B. Cunningham, and K. N. Salama, "Numerical modeling for terahertz testing of non-metallic pipes," *AIP Adv.*, vol. 10, no. 9, Sep. 2020, Art. no. 095112.

[20] *Altair FEKO*. Accessed: Dec. 14, 2021. [Online]. Available: https://www.altair.com/feko/

[21] A. Al-Ghamdi *et al.*, "Dielectric and microwave properties of polyvinyl chloride/graphite/nickel composites and its applications," *J. Thermoplastic Compos. Mater.*, vol. 27, no. 4, pp. 528–540, Apr. 2014.

[22] MATLAB, *Version 9.10.0.1710957 (R2021a)*. Natick, MA, USA: MathWorks, 2021.

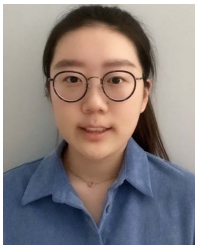

Yuki Gao (Member, IEEE) received the B.S. degree (*summa cum laude)* in electrical and computer engineering from the New York Institute of Technology (New York Tech), New York, NY, USA, in 2021, where she is currently pursuing the M.Sc. degree in electrical and computer engineering under the Accelerated Program.

She has been a Research Assistant with the Applied Electromagnetics Research Laboratory, New York Tech, since 2019. Her research interests include nondestructive testing, microwave holographic imaging, microwave sensing, image reconstruction, and biomedical imaging.

Maharshi B. Shah received the M.Sc. degree in electrical and computer engineering from the New York Institute of Technology (New York Tech), New York, NY, USA, in 2014, where he is currently pursuing the Ph.D. degree in electrical engineering with the Applied Electromagnetics Research Laboratory.

He is currently working as a Research Assistant with the Applied Electromagnetics Research Laboratory, New York Institute of Technology. His research interests include nondestructive testing, microwave holographic imaging techniques, RF and microwave circuit design, and image reconstruction.

Reza K. Amineh (Senior Member, IEEE) received the Ph.D. degree in electrical engineering from McMaster University, Hamilton, ON, Canada, in 2010.

He was the Principal Scientist of the Department of Sensor Physics, Halliburton Company, Houston, TX, USA. He was a Post-Doctoral Fellow with the University of Toronto, Toronto, ON, Canada, and McMaster University, from 2010 to 2013. He was a Ph.D. Intern with the Advanced Technology Group, BlackBerry, Waterloo, ON, Canada, in 2009. He is currently an Assistant Professor with the Department of Electrical and Computer Engineering, New York Institute of Technology, New York, NY, USA. He has authored/coauthored more than 80 journal articles and conference papers, two book chapters, and a book titled *Real-Time Three-Dimensional Imaging of Dielectric Bodies Using Microwave/Millimeter Wave Holography* (Wiley & IEEE Press). He has contributed to more than 40 patent disclosures in applied electromagnetics while working at Halliburton Company and received several industrial awards. His research interests include applied electromagnetics with applications in imaging and sensing.

Dr. Amineh was a recipient of the Banting Post-Doctoral Fellowship in Canada in 2012 and the Ontario Ministry of Research and Innovation (OMRI) Post-Doctoral Fellowship in 2010. During his Ph.D. program, he received the McMaster Internal Prestige Scholarship Clifton W. Sherman for two consecutive years. He has coauthored a paper selected as a finalist in the Student Paper Competition at IEEE Wireless and Microwave Technology Conference in 2019, the Honorable Mention Paper presented at the IEEE Symposium on Antennas and Propagation in 2008, and a paper selected among the *Inverse Problems* journal "Highlights Collection of 2010."